SUPPLEMENTARY MATERIAL

Titanite as a recorder of polymetamorphism: Integrated U-Pb geochronology, single element thermometry, and major and trace element chemistry

Jesse B. Walters[1,2], Alicia M. Cruz-Uribe[2], Won Joon Song[2], Christopher Gerbi[2], Kimberley Biela[3]

[1]Institut für Geowissenschaften, Goethe Universität, Frankfurt am Main 60438, Germany
[2]School of Earth and Climate Sciences, University of Maine, Orono 04469, United States
[3]Anthropology and Geography, Colorado State University, Fort Collins 80521, United States

APPENDIX S1 MAJOR AND MINOR ELEMENT ANALYSIS BY EPMA

Major and minor element data on silicate phases were collected through electron probe microanalysis (EPMA) using a Cameca SX-100 electron microprobe equipped with five wavelength dispersive spectrometers, housed at the University of Maine. Standard spot analyses utilized a beam size of 5 μm, accelerating voltage of 15 keV, and 10 nA beam current. On-peak counting times were 20 s for all elements, except for Na, where counting time was 10 s. Backgrounds were measured for half the on-peak counting time. Data are reported in Table S1 as the mean and 2SE of multiple analyses collected within compositionally homogenous domains. Ferric iron in garnet and clinopyroxene was determined using method #2 of Schumacher (1991), in which all Fe is considered Fe^{3+} in titanite and epidote-group minerals. Amphibole structural formula calculations follow Leake et al. (1997) and classified following Hawthorne *et al*. (2012). Structural formulae of other minerals were determined by assuming a total number of cations or anions where appropriate and the methods listed are given in Appendix S1.

Qualitative and quantitative compositional maps were also collected by EPMA. Qualitative garnet (Fig. S3) and full thin section (Fig. S6) X-ray intensity maps were collected using a 20 keV accelerating voltage, 100 nA beam current, and a dwell time of 30 ms. Single- and multi-phase quantitative maps were collected using at a 15 keV accelerating voltage, 100 nA beam current, and 300 ms dwell time with a focused beam and a step size of 2 μm. X-ray intensity maps were quantified using 15–36 spot analyses per phase and the program XMapTools (Lanari *et al.*, 2014; 2018).

APPENDIX S2 MAJOR MINERAL LA-ICP-MS ANALYSIS

In addition to titanite, minor and trace element analyses (Session 3) were conducted on diopside, amphibole, epidote group minerals, plagioclase, and alkali feldspar and are reported in Table S7. Analyses of diopside, amphibole, and epidote group minerals were conducted with a spot diameter of ~ 30 or ~ 40 μm, a ~ 3 J cm^{-2} beam energy density, and a repetition rate of 8 Hz, whereas feldspar analyses were conducted with a 40 μm spot diameter, a 6.7 J cm^{-2} beam energy density, and a repetition rate of 8 Hz. A gas flow rate of 800 mL/min of He was used, and a 'Squid'-type signal smoother was employed. Measured isotopes and dwell times (ms) were ^{27}Al (3), ^{29}Si (3), ^{44}Ca (3), ^{49}Ti (30), ^{56}Fe (20), ^{88}Sr (14), ^{89}Y (5), ^{90}Zr (10), ^{93}Nb (10), ^{137}Ba (20), ^{139}La (20), ^{140}Ce (15), ^{141}Pr (20), ^{146}Nd (20), ^{147}Sm (20), ^{153}Eu (20), ^{157}Gd (20), ^{159}Tb (20), ^{163}Dy (20), ^{165}Ho (20), ^{166}Er (20), ^{169}Tm (20), ^{172}Yb (20), ^{175}Lu (20), ^{178}Hf (20), ^{181}Ta (20), and ^{208}Pb (10). All analyses consisted of 40 s ablation with 15 s background collection during laser warm up and 10 s of washout on the ICP-MS. Unknown analyses were bracketed with analyses NIST SRM610, NIST SRM612, and GSD1G reference glasses. We used NIST SRM610 as the primary reference material and the data were reduced using Iolite (v4). Silicon contents measured by EPMA were used as the internal standards and are reported in Table S7. Trace element concentrations for plagioclase and amphibole were calculated using compositional extremes. Major mineral LA-ICP-MS results are summarized in Table S7.

APPENDIX S3 ELECTRON BACKSCATTER DIFFRACTION ANALYSIS

For electron backscatter diffraction (EBSD) analysis of titanite grains in Sample SSP18-1A, the sample was polished mechanically with 0.3 μm alumina suspension and chemically in 0.02 μm colloidal silica suspension, and then was coated with a thin layer of carbon to prevent electron charging. EBSD patterns of titanites were collected in the Tescan Vega II Scanning Electron Microscope equipped with an EDAX-TSL EBSD system at the University of Maine. Operating conditions for the EBSD analysis were an acceleration voltage of 20 kV, a working distance of 25 mm, a beam current of ~6 nA, a 70° sample tilt, high-vacuum conditions, and a step size of 2 μm.

Collected EBSD patterns were indexed using the crystallography data of a natural titanite sample (E2312; Hawthorne *et al*., 1991). EDAX-TSL OIM Analysis 6 software was used to post-process titanite EBSD data based on confidence index (CI) and neighboring orientations. Non- and poor-indexed pixels (CI < 0.02) were replaced with well-indexed neighboring pixels of CI ≥0.02. The indexing rate is more than 99.8 %. Relative misorientation maps display the minimum misorientation relative to a reference orientation (see Figs. S7–S8), whereas the kernel average misorientation maps show the average misorientation (between 0 to 2 °C) for up to the 3rd neighbor (Fig. S9).

APPENDIX S4 PETROGRAPHY OF PARAGNEISS SAMPLE SSP18-1D

Sample SSP18-1D is a paragneiss with the peak assemblage Grt + Bt + Pl + Qtz + Sil + Kfs (Fig. S2). Garnets are relatively small (<2 mm) and range in composition from $Alm_{75}Prp_{13}Sps_{10}Adr_2$ in the core to $Alm_{68}Prp_9Sps_{20}Adr_3$ in the rim. X-ray maps and core-to-rim transects show Fe-Mg zoning consistent with diffusional resetting and retrograde net-transfer reactions during cooling (Fig. S3 & S4). Biotite inclusions in garnet exhibit are more magnesian (X_{Mg} = 0.45–0.54) relative to matrix grains (X_{Mg} = 0.39–0.42) and are lower in Ti content (0.00–0.151 APFU compared to 0.181–0.209 APFU). Sillimanite intergrown with biotite is observed as inclusions in garnet (Fig. S2a). Additionally, muscovite is not observed as inclusions in garnet. These observations are consistent with the muscovite dehydration and melting reaction:

(S1) Ms + Pl + Qtz = Kfs + Sil + Bt + L.

Two types of overprinting textures are noted in the matrix. First, muscovite is commonly associated with biotite, whereas sillimanite is not observed, and alkali-feldspar is relatively rare. These data suggest sillimanite and alkali feldspar were consumed to produce retrograde muscovite during cooling, either by the recrystallization of partial melts or an influx of H_2O-rich fluids. Plagioclase rims are also locally recrystallized: An contents decrease from a maximum of 30 in the cores to 20 in the rims.

APPENDIX S5 MAJOR ELEMENT THERMOBAROMETRY

Major element thermobarometry was conducted on the measured extreme compositions of garnet, biotite, and plagioclase in sample SSP18-1D. Garnet-biotite temperatures were calculated

using the calibration of Ferry & Spear (1976) with the Berman (1990) garnet activity model. For garnet core assemblages, the upper pressure limit was calculated using the garnet-aluminosilicate-quartz-plagioclase (GASP) barometer using the calibration of Hodges & Crowley (1985). The lower pressure limit is given by the garnet-biotite-quartz-plagioclase barometers (R1 & R2) of Hoisch (1990). Temperatures are rounded to the nearest 5 degrees and pressures are rounded to the nearest 10 MPa.

Garnets exhibit core to rim decreases in both X_{Alm} and X_{Prp}, rimward increases in X_{Sps} and X_{Fe}, and a flat profile in X_{Grs} (Figs. S3 & S4). Rimwards decreases in both Fe and Mg are consistent with retrograde net transfer reactions whereas the rimward increase in X_{Fe} is the result of diffusive retrograde Fe-Mg exchange between garnet and biotite (Spear, 1991; Kohn & Spear, 2000). If garnet compositions were only perturbed by Fe-Mg exchange, analyses of low X_{Fe} garnet cores and matrix biotite would result in the best estimate of the minimum peak temperature (Kohn & Spear, 2000). In our sample, this approach gives an estimate of ~900 °C at 500 MPa; however, cordierite, orthopyroxene, and more significant partial melting would be expected under these conditions (Fig. S14). In contrast, *P–T* estimates for garnet rims and adjacent matrix phases give P-T conditions of 595–655 °C (Fig. S14) and 240–520 MPa using the garnet-biotite thermometer with the barometers of Hoisch (1990). These estimates overlap with the regional *P–T* range calculated by Holdaway *et al.* (1997) but are below the vapor-present muscovite-out melting reaction, inconsistent with widespread migmatization in the region and sillimanite inclusions in garnet (Fig. S14).

Magnesium X-ray maps and spot analyses reveal elevated Mg in biotite inclusions relative to the matrix. Three different garnet-biotite inclusion pairs were used, whereas plagioclase inclusions are rare and only a single inclusion was measured and applied to the pressure calculation for each of the three garnets (Fig. S3). The *P–T* range calculated for the smaller and more strongly retrogressed garnets is 300–530 MPa and 545–630 °C (Fig. S3a–f & S14) and are again inconsistent with the extensive migmatization observed by us and others in this region. In contrast, a third larger garnet (Fig. S3g–i) exhibits the range 630–700 MPa and 725–740 °C (Fig. S14). This estimate overlaps with the estimate of 620 MPa and 700 °C by Holdaway, Dutrow, & Hinton (1988) for metapelite sampled near our locality. The high *P–T* estimate is consistent with the muscovite dehydration and melting in the metapelites, and the Di + An + Cal + Ttn peak assemblage for the calc-silicate layers (Fig. 10). Therefore, we suggest that 630–700 MPa and 725–740 °C is the most accurate *P–T* estimation for the metamorphic peak.

SUPPLEMENTARY REFERENCES

Berman, R.G. (1990). Mixing properties of Ca-Mg-Fe-Mn garnets. *American Mineralogist*, 75, 328-344.

Ferry, J.M., & Spear, F.S. (1978). Experimental calibration of the partitioning of Fe and Mg between biotite and garnet. *Contributions to Mineralogy and Petrology*, 66, 113-117.

Hawthorne, F.C., Groat, L.A., Raudsepp, M., Ball, N.A., Kimata, M., Spike, F.D., … McCammon, C. (1991). Alpha-decay damage in titanite. *American Mineralogist*, 76, 370-396.

Hawthorne, F.C., Oberti, R., Harlow, G.E., Maresch, W.V., Martin, R.F., Schumacher, J.C., & Welch, M.D (2012). Nomenclature of the amphibole supergroup. *American Mineralogist*, 97, 2031-2048.

Hodges, K.V., & Crowley, P.D. (1985). Error estimation and empirical geothermobarometry for pelitic systems. *American Mineralogist*, 70, 702-709.

Hoisch, T.D. (1990). Empirical calibration of six geobarometers for the mineral assemblage quartz +muscovite + biotite + plagioclase + garnet. *Contributions to Mineralogy and Petrology*, 104, 225-234.

Holdaway, M.J, Dutrow, B.L., & Hinton, R.W. (1988). Devonian and Carboniferous metamorphism in west-central Maine: The muscovite-almandine geobarometer and the staurolite problem revisited. American Mineralogist, 73, 20-47.

Holdaway, M.J., Mukhapodhyay, B., Dyar, M.D., Guidotti, C.V., & Dutrow, B.L. (1997). Garnet-biotite geothermometry revised: New Margules parameters and a natural specimen data set from Maine. American Mineralogist, 82, 582-595.

Kohn, M.J., & Spear, F.S. (2000). Retrograde net transfer reaction insurance for pressure-temperature estimates. *Geology*, 28, 1127.
Lanari, P., Vidal, O., de Andrade, V., Dubacq, B., Lewin, E., Grosch, E.G., Schwartz, S. (2014). XMapTools: A MATLAB©-based program for electron microprobe X-ray image processing and geothermobarometry. *Computers & Geosciences*, 62, 227-240.

Lanari, P., Vho, A., Bovay, T., Airaghi, L., Centrella, S. (2018). Quantitative compositional mapping of mineral phases by electron probe micro-analyser. *Geological Society of London, Special Publications*, 478, 39-63.

Leake, B.E., Woolley, A.R., Arps, C.E.S., Birch, W.D., Gilbert, M.C., Grice, J.L., … Youzhi, G. (1997). Nomenclature of Amphiboles: Report on the subcommittee on amphiboles of the International Mineralogical Association, Commission on New Minerals and Mineral Names. *American Mineralogist*, 82, 1019-1037.

Schumacher, J. (1991). Empirical ferric iron corrections: Necessity, assumptions, and effects on selected geothermobarometers. *Mineralogical Magazine*, 55, 3-18.

Spear, F.S. (1991). On the interpretation of peak metamorphic temperatures in light of garnet diffusion during cooling. *Journal of Metamorphic Geology*, 9. 379-388.

Spear, F.S., Kohn, M.J., & Cheney, T.J. (1999). P-T paths from anatectic pelites. *Contributions to Mineralogy and Petrology*, 134, 17-32.

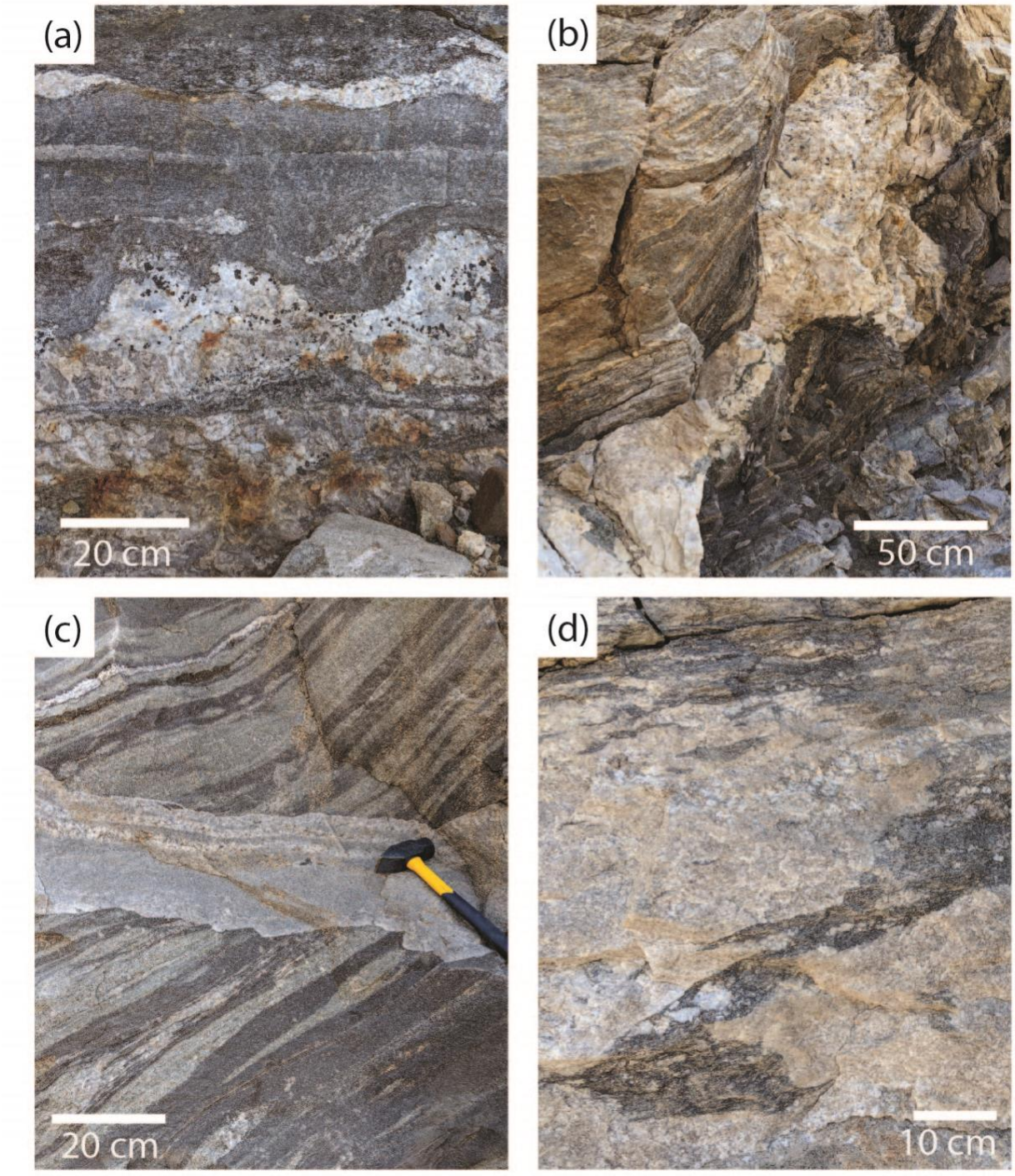

Figure S1. Field photographs of deformed syn- or pre-deformational granite dikes (a–b) and undeformed granite dikes which cross-cut the foliation (c–d). Host rocks include a gneiss with alternating bands of calcsilicate and metapsammite (c) and migmatite (b & d). Sample SSP18-1A shows characteristics similar to the bands shown in c.

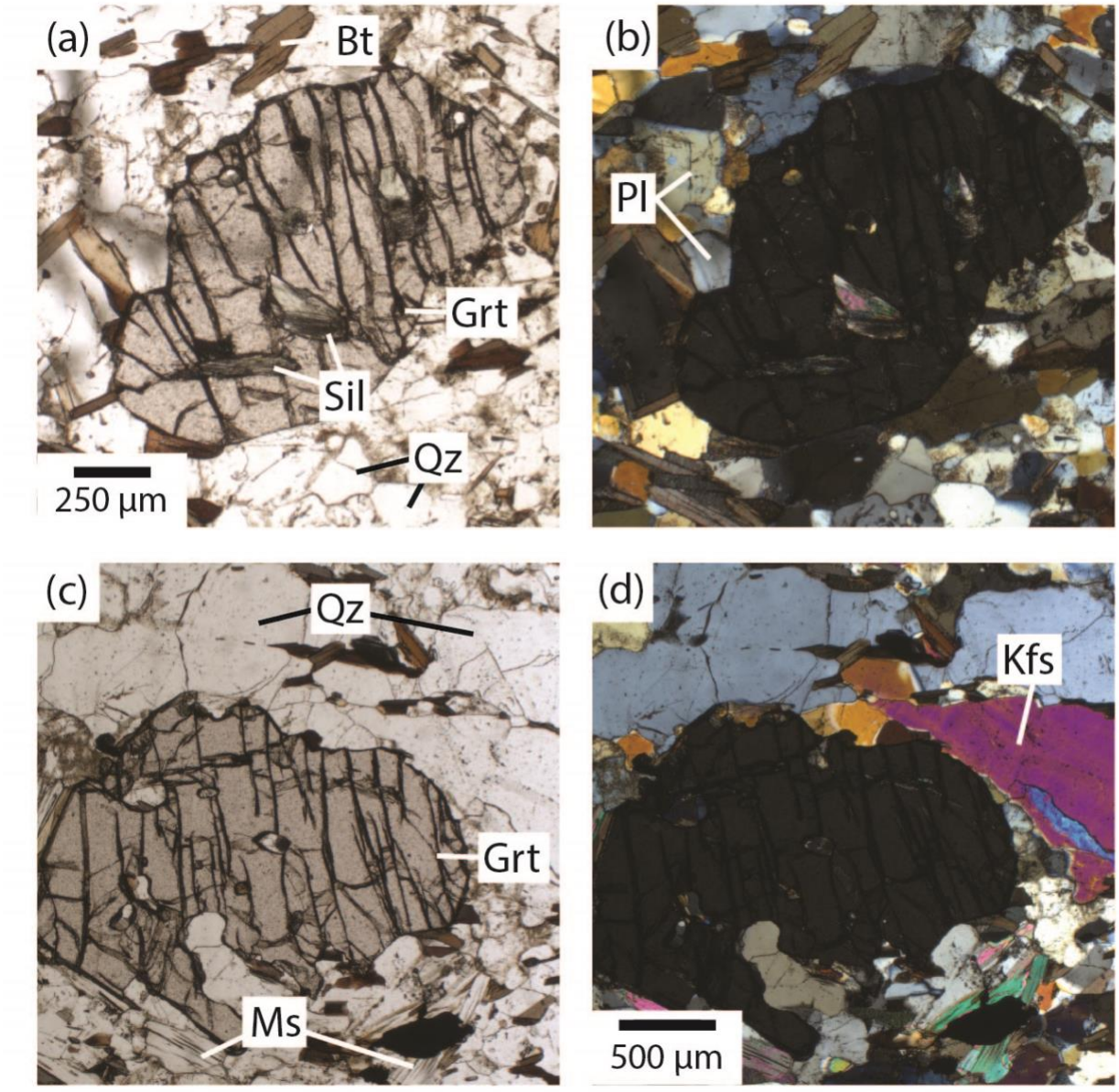

Figure S2. Transmitted plane polarized light (a & c) and cross polarized light (b & d) photomicrographs of sample SSP18-1D. Sillimanite is observed as inclusions in garnet porphyroblasts (a) and muscovite, quartz, plagioclase, biotite, and alkali feldspar make up the matrix (a–d).

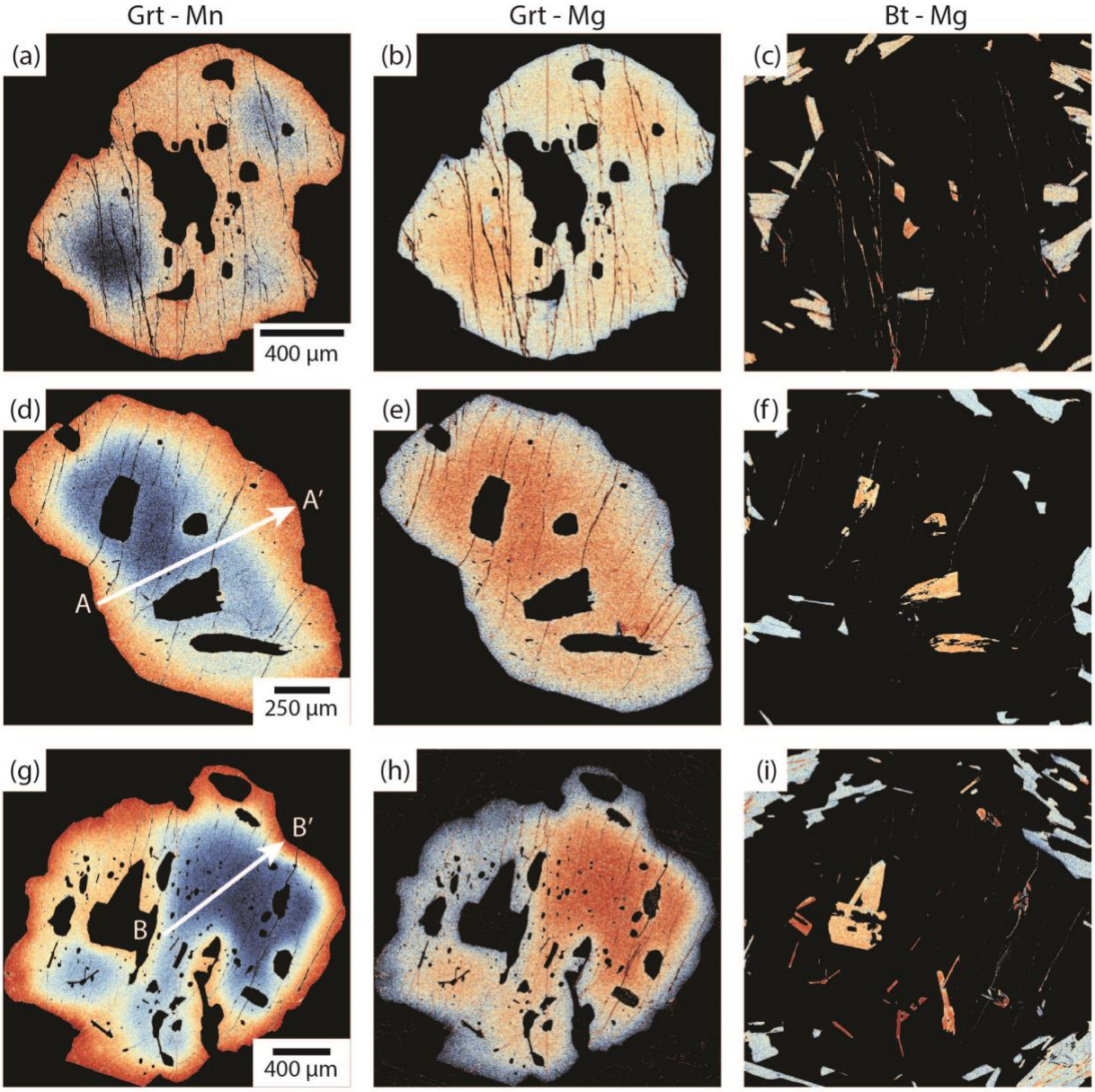

Figure S3. X-ray intensity maps of Mn in garnet (a, d, g), Mg in garnet (b, e, h), and Mg in biotite (c, f, i) in metapelite sample SSP18-1D. Arrows indicate the position and direction of EPMA transects in Fig. S4.

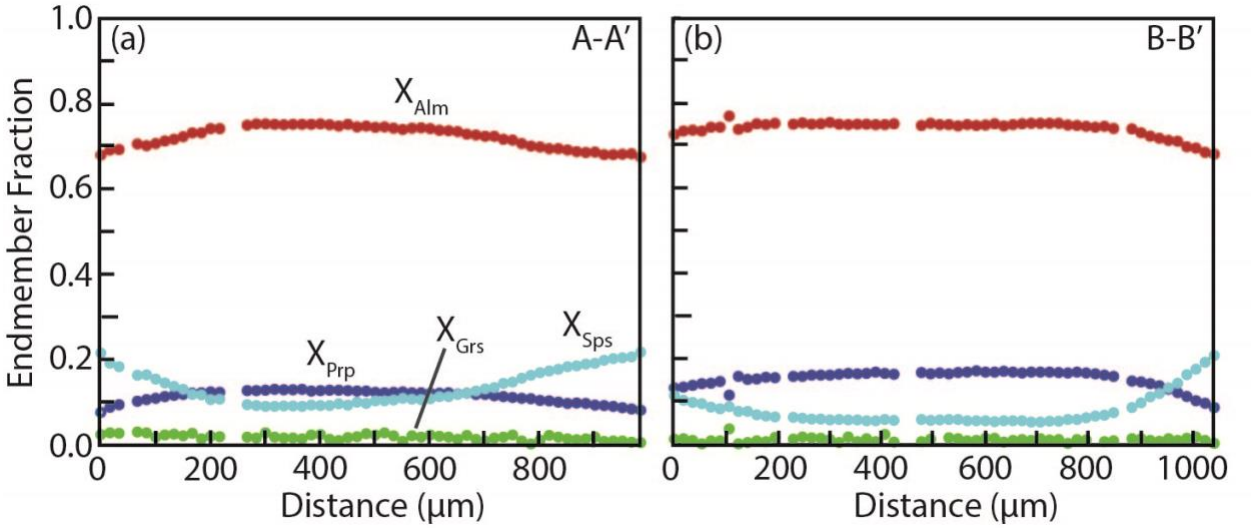

Figure S4. Transections of the mole fraction of almandine, grossular, pyrope, and spessartine from two garnets from A-A` (a) and B-B` (b) in sample SSP18-1D. Transect locations are shown in Fig. S3.

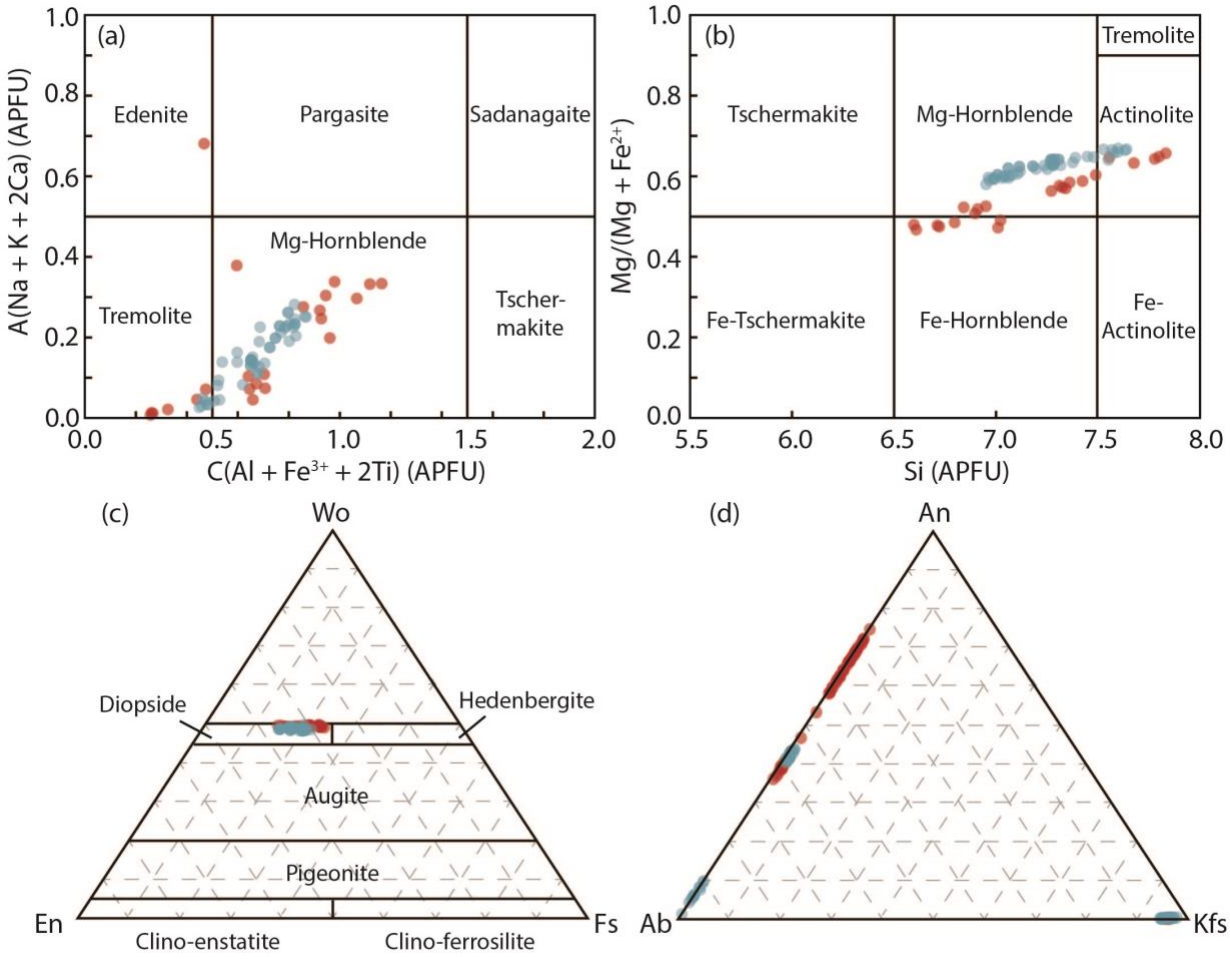

Figure S3. Plots of amphibole (a & b), pyroxene (c), and feldspar (d) compositions measured by EPMA in samples SSP18-1A (blue) and SSP18-1B (red).

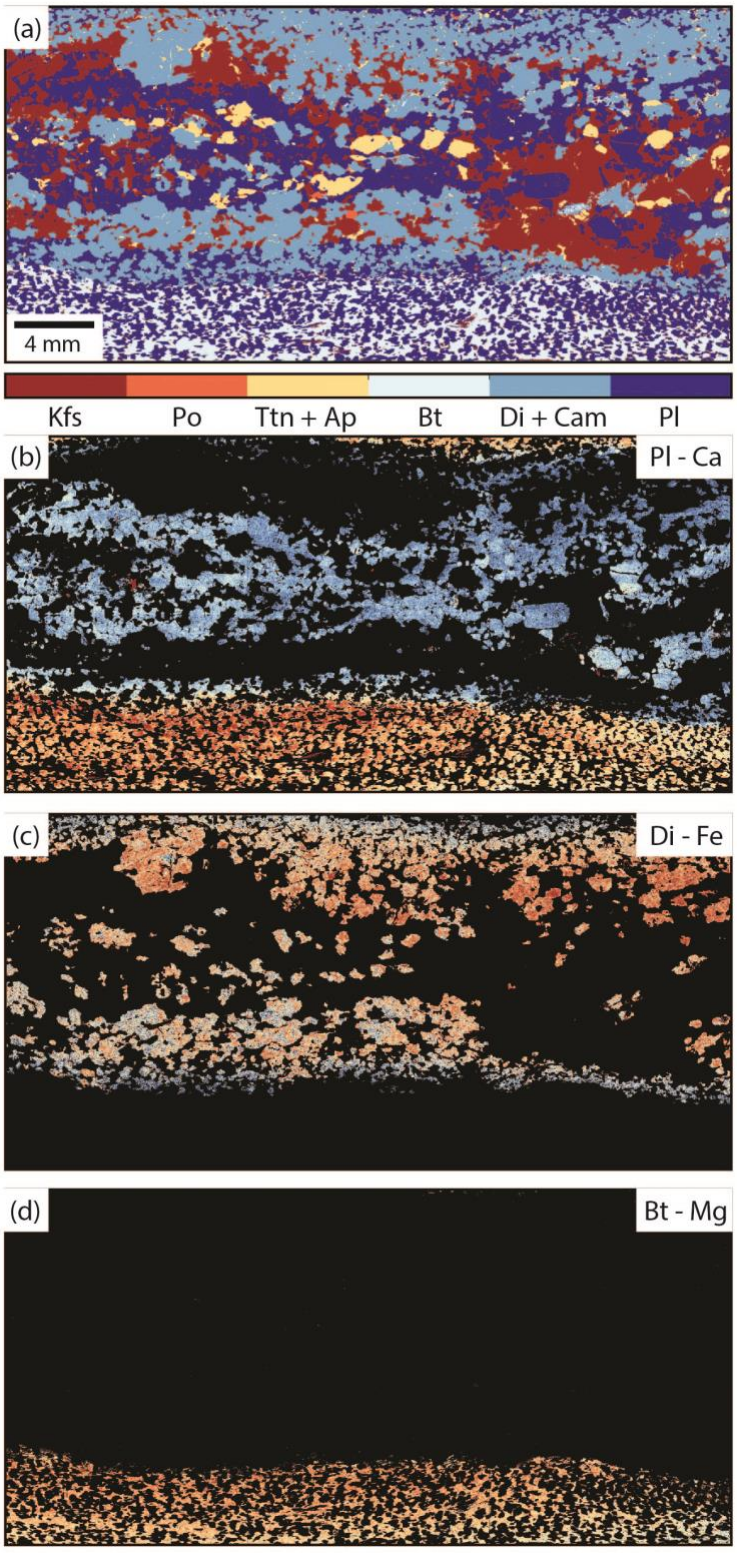

Figure S6. Full thinsection mineral mode map (a) and X-ray intensity scans of Ca in plagioclase (b), Fe in diopside (c), and Mg in biotite (d) from sample SSP18-1A. The lower biotite- and plagioclase-rich region is a metapsammitic band, whereas the upper region is a calcsilicate band.

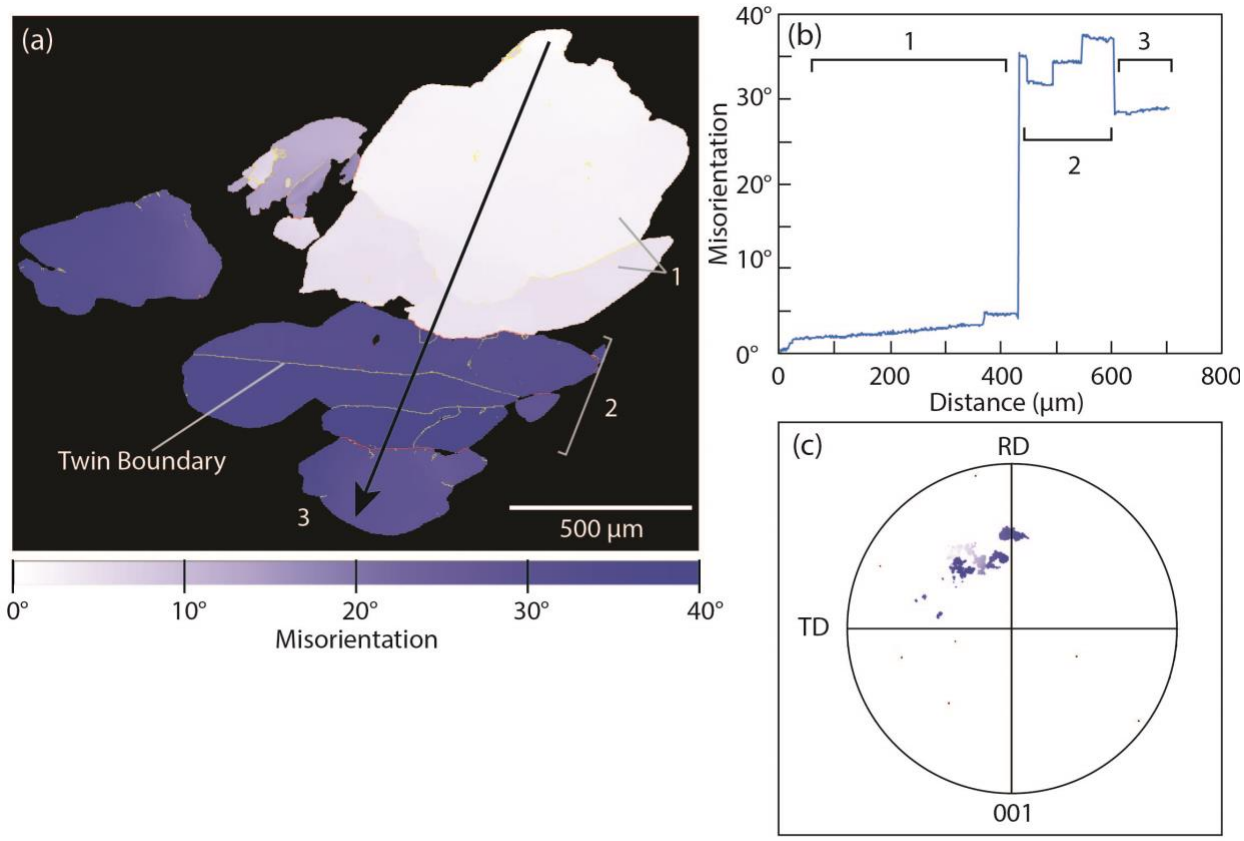

Figure S4. Relative misorientation map (a), misorientation profile (b), and pole figure (c) showing the poles of the {001} crystallographic planes at each pixel in (a) using an upper hemisphere, equal area projection for titanite (grain 1) from Sample SSP18-1A. The color of each pixel in (a and c) is defined relative to a user defined reference orientation. Red lines correspond to high angle (> 10°) boundaries, whereas yellow lines correspond to low angle boundaries (between 1 and 10°).

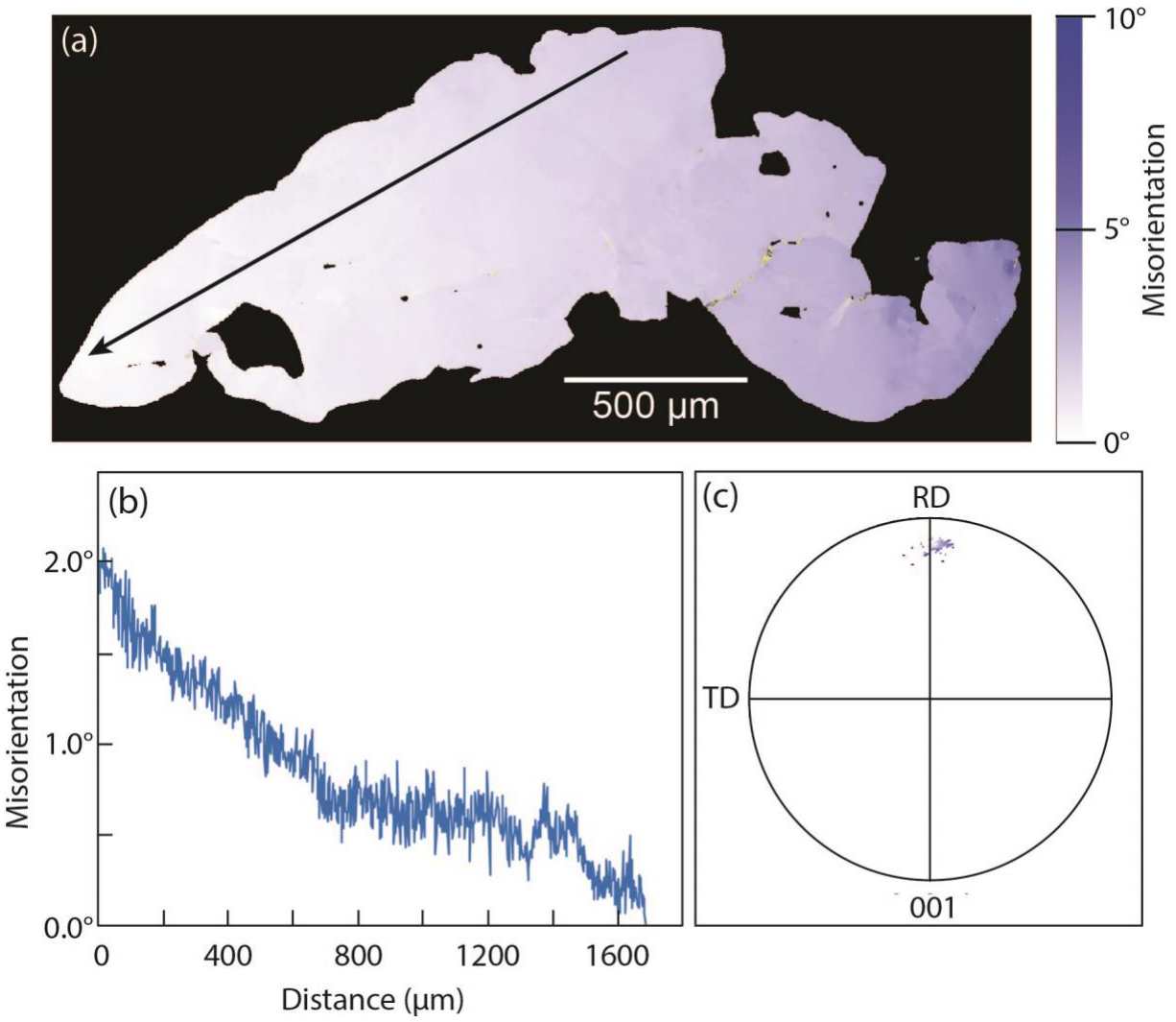

Figure S5. Relative misorientation map (a), misorientation profile (b), and pole figure (c) showing the poles of the {001} crystallographic planes at each pixel in (a and c) using an upper hemisphere, equal area projection for titanite (grain 1) from Sample SSP18-1A. The color of each pixel in (a) is defined relative to a user defined reference orientation. Red lines correspond to high angle (> 10°) boundaries, whereas yellow lines correspond to low angle boundaries (between 1 and 10°).

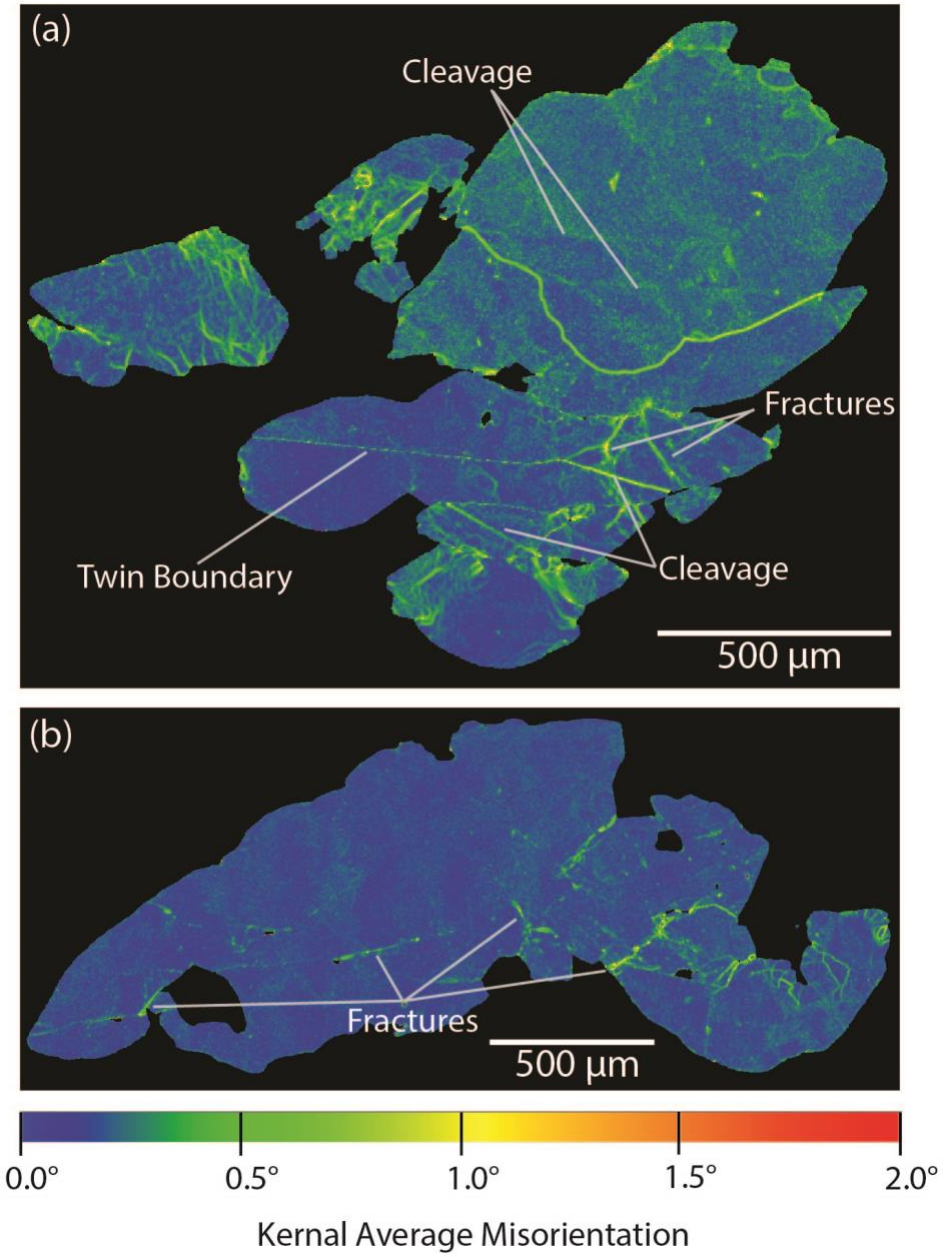

Figure S*9*. Kernel average misorientation maps for titanite grains 1 (a) and 2 (b) in SSP18-1A. The misorientation is calculated up to the third neighbor with a 2° threshold angle.

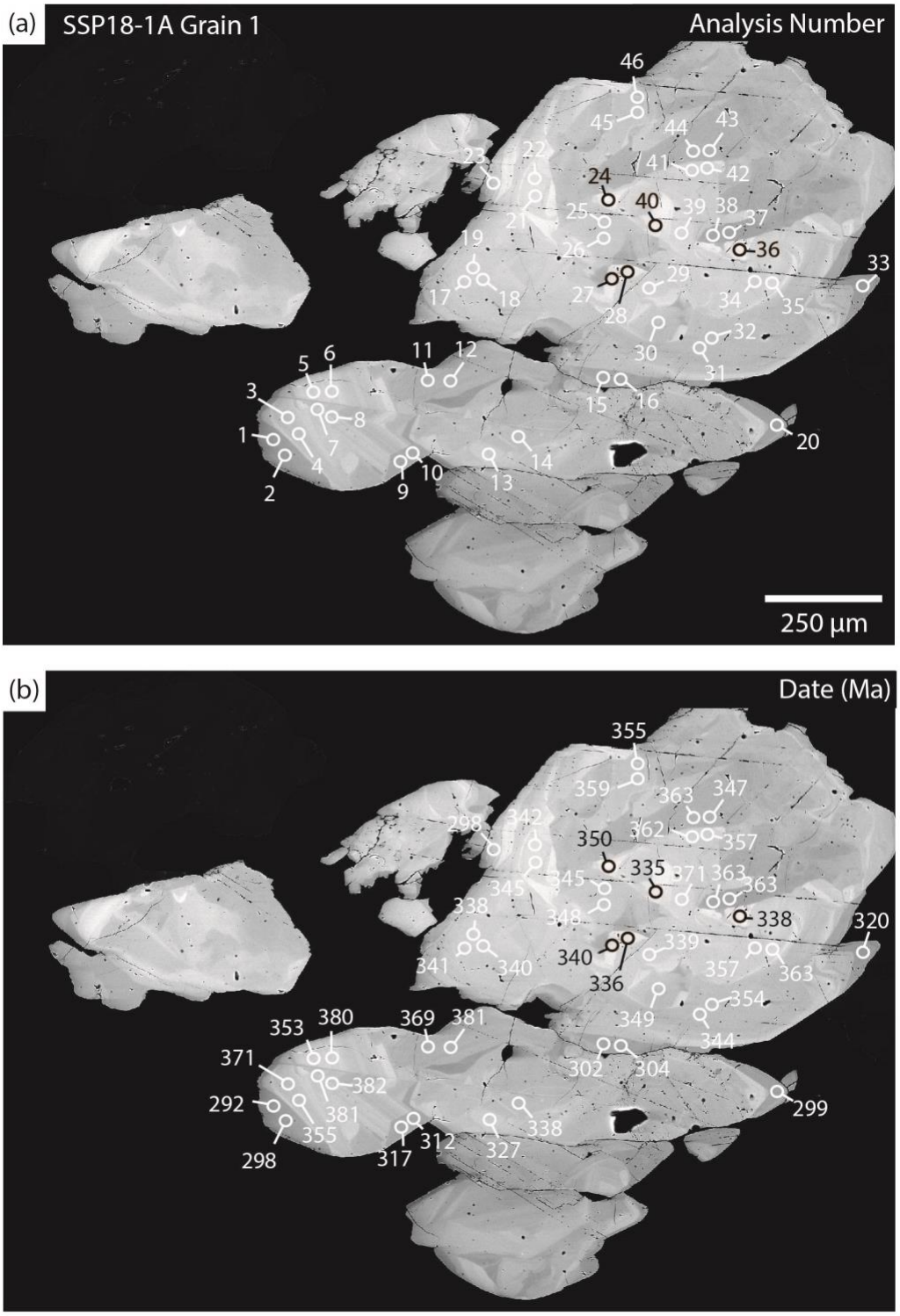

Figure S10. BSE images of titanite (grain 1) from SSP18-1A with LA-ICP-MS analysis locations (A) and single-spot dates (B) shown.

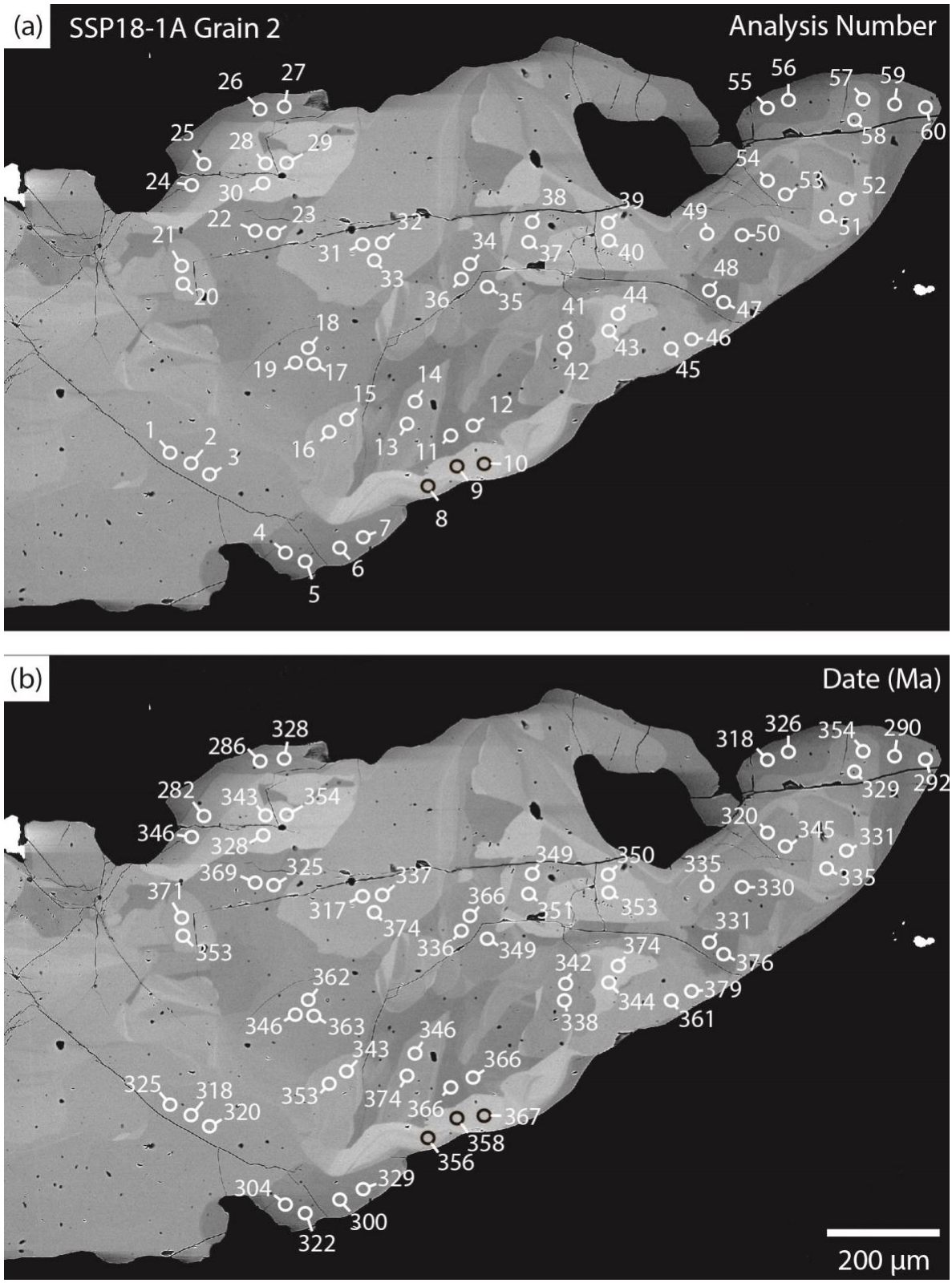

Figure S6. BSE images of titanite (grain 2) from SSP18-1A with LA-ICP-MS analysis locations (a) and single-spot dates (b) shown.

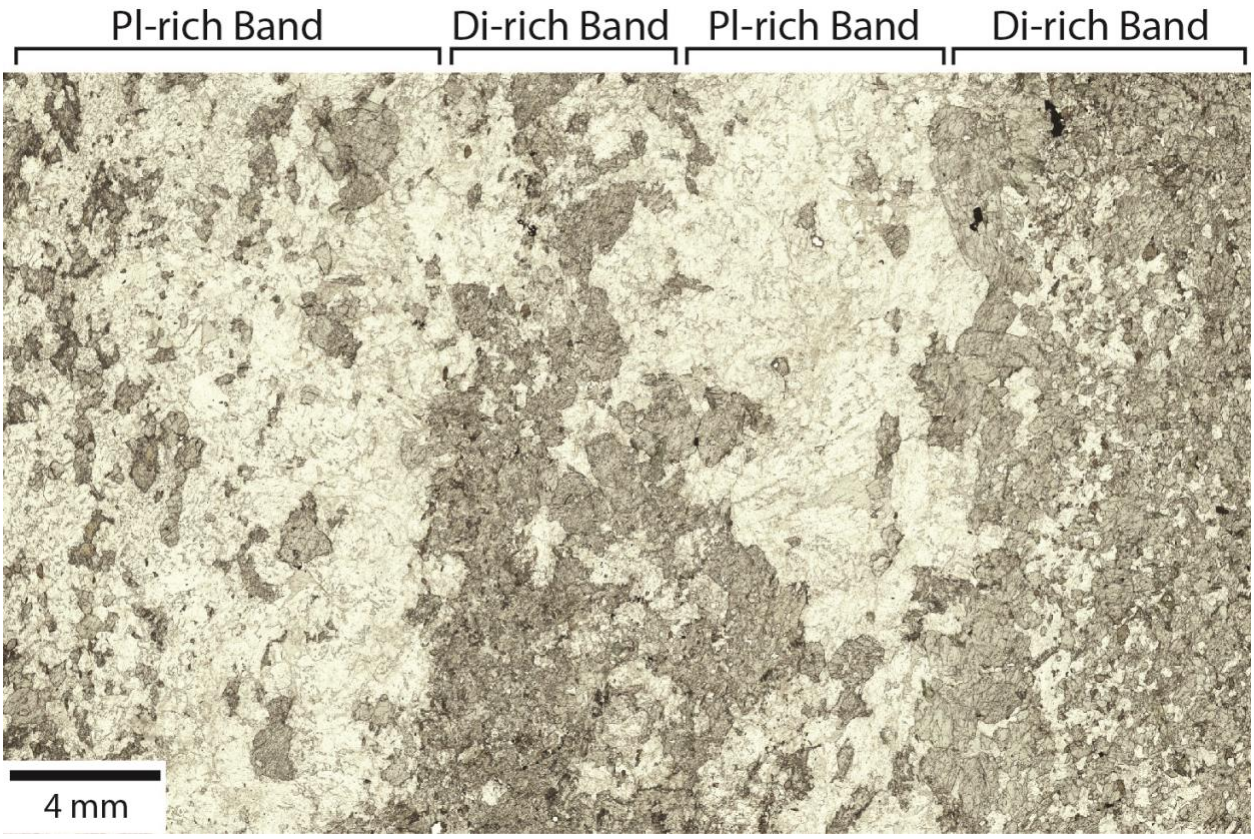

Figure S2. Full thin section photomicrograph of sample SSP18-1B illustrating alternating plagioclase- and diopside-rich bands.

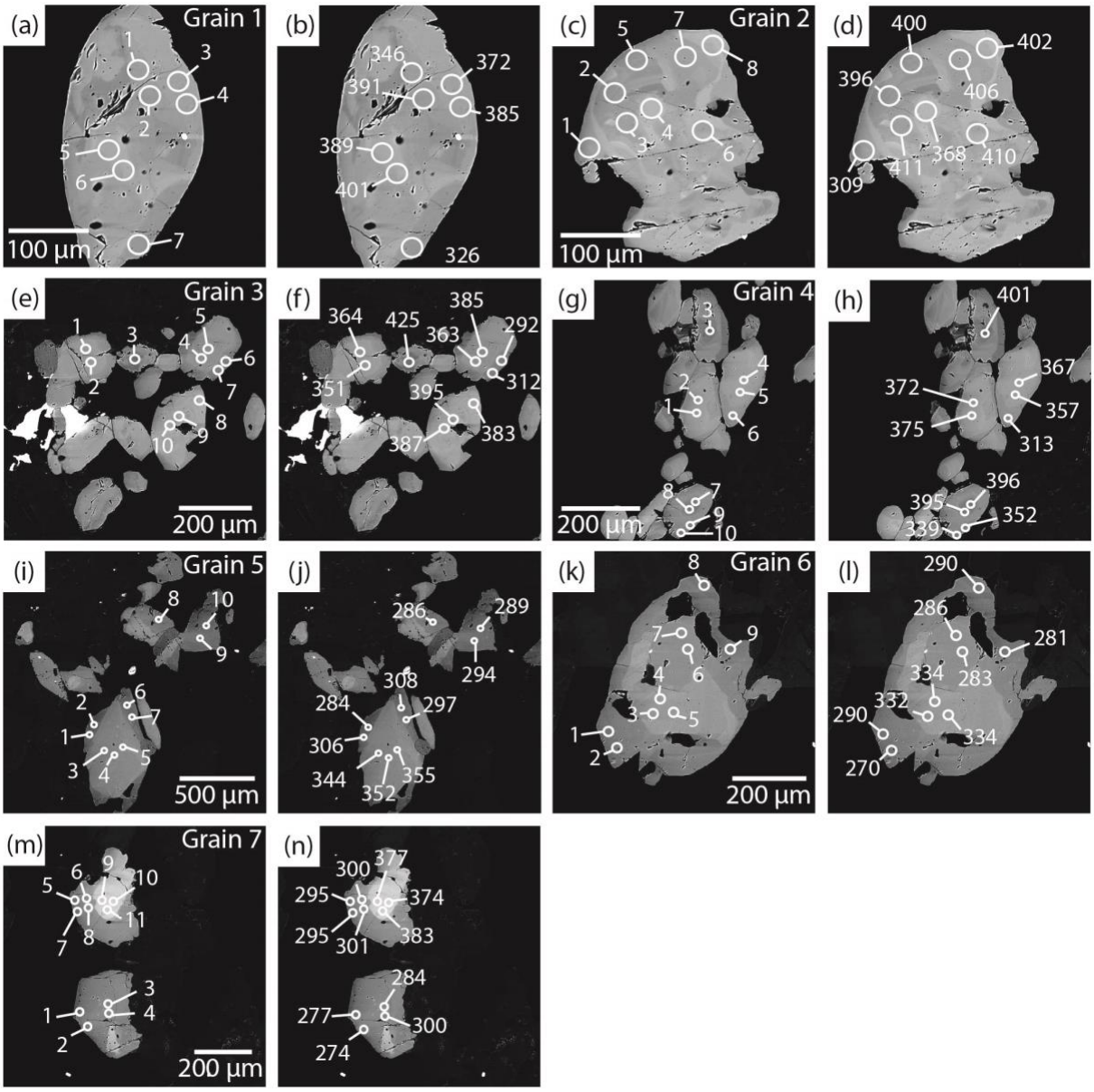

Figure S13. BSE images of titanite (grains 1–7) from SSP18-1B with LA-ICP-MS analysis locations (a, c, e, g, i, k, m) and dates (b, d, f, h, j, l, n) shown.

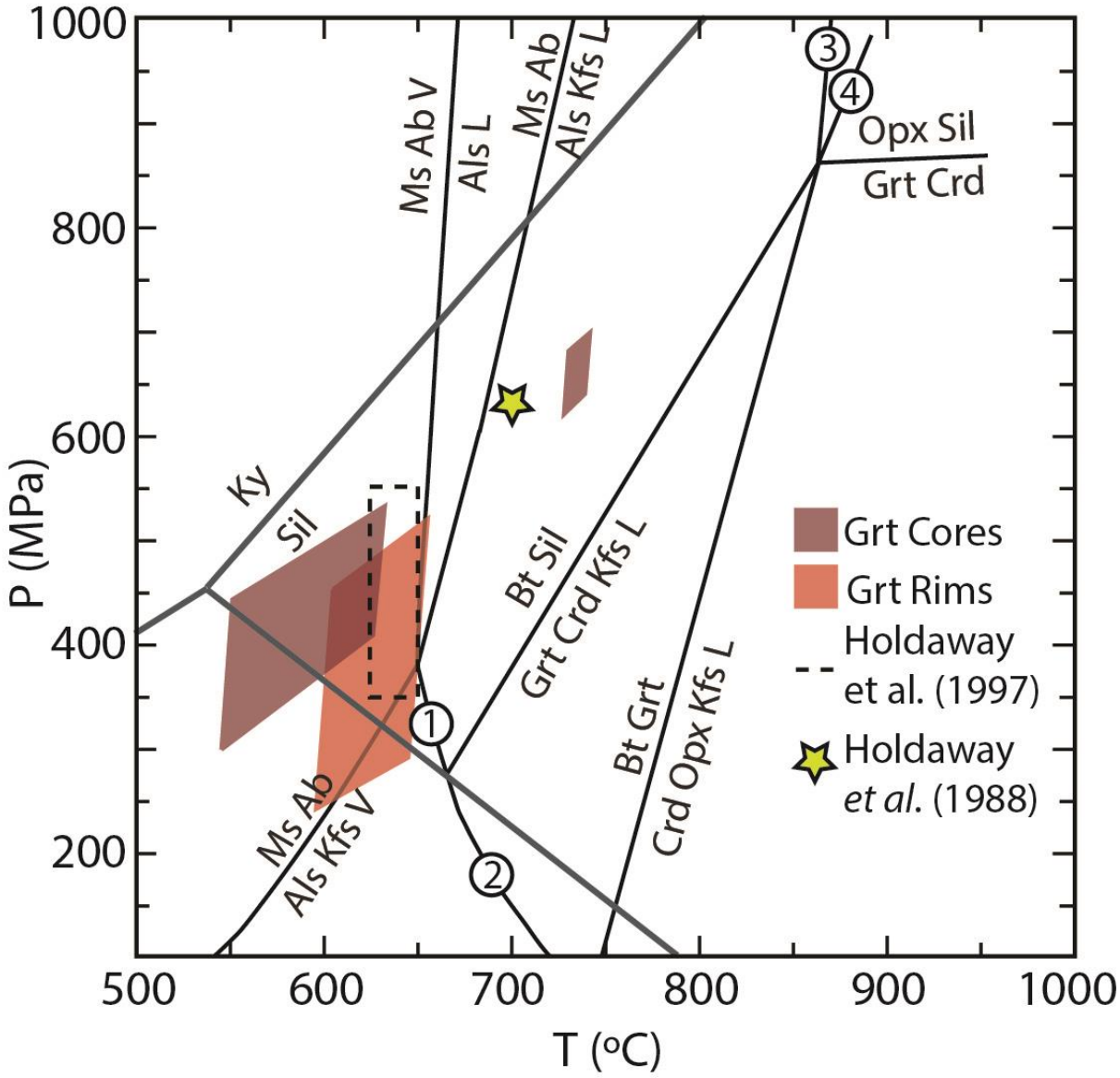

Figure S7. Diagram showing *P–T* estimates calculated from garnet cores and inclusion pairs (dark red), as well as garnet rims and matrix minerals (light red). The *P–T* estimates of Holdaway, Dutrow, & Hinnton (1988) and Holdaway *et al.* (1997) are also shown. The core of the least reset garnet (Fig. S2G & H) gives a higher *P–T* relative to other garnets. Petrographic grid in the NKFMASH system modified after Spear, Kohn, & Cheney (1999). Als: aluminosilicate, V: vapor, L: melt. Numbered reactions correspond to Kfs + Als = L (1), Grt + Ab + Kfs + Crd + Bt + V = L (2), Bt + Grt = Opx + Als + L (3), and Bt + Als = Opx + Crd + L (4).